Thin Solid Films 636 (2017) 359–366

Contents lists available at ScienceDirect

Thin Solid Films

journal homepage: www.elsevier.com/locate/tsf

Facile and controllable fabrication of multifunctional nanohybrid films composed of reduced graphene oxide and titanium dioxide through layer-by-layer assembly

Young-Kwan Kim [a,*], Hongje Jang [b], Kyungtae Kang [c]

[a] Carbon Composite Materials Research Center, Institute of Advanced Composite Materials, Korea Institute of Science and Technolgy, San 101, Eunha-ri, Bongdong-eup, Wanju-gun, Jeollabuk-do 565-905, Republic of Korea
[b] Department of Chemistry, Kwangwoon University, 20, Gwangwoon-ro, Nowon-gu, Seoul 139-701, Republic of Korea
[c] Department of Applied Chemistry, Kyung Hee University, Yongin, Gyeonggi 446-701, Republic of Korea

ARTICLE INFO

Article history:
Received 6 March 2017
Received in revised form 16 May 2017
Accepted 24 June 2017
Available online 26 June 2017

Keywords:
Graphene oxide
Hybrid films
Layer-by-layer assembly
Surface modification
Titanium (IV) bis(ammonium lactato) dihydroxyde
Self-cleaning
UV protection
Transparent electrode

ABSTRACT

A facile fabrication strategy of multi-functional hybrid thin films of reduced graphene oxide (RGO) and TiO_2 was developed by using layer-by-layer (LBL) assembly of titanium(IV) bis(ammonium lactato)dihydroxide (TALH) and polyallylamine grafted reduced graphene oxide (PAA-RGO) as negatively and positively charged components. The fabrication process of hybrid films was thoroughly characterized by using UV–vis spectroscopic, ellipsometric and atomic force microscopic analysis. This fabrication strategy provided precisely-controlled thickness, surface roughness through 1–10 LBL assembly cycles. By thermal treatment, the PAA-RGO and TALH in the hybrid films were respectively converted into RGO and TiO_2 with the restoration of their electrical conductivity, UV-resistance and photo-catalytic self-cleaning properties.

1. Introduction

Graphene, single layered sp^2 carbon network, has attracted much attention because of its unique chemical, mechanical and electrical properties [1]. Graphene oxide (GO) is an oxidized form of graphene presenting various oxygen containing functional groups, dispersible in water, and convertible into reduced GO (RGO) by chemical and thermal reduction [2]. In addition, GO possesses unique properties distinguishable from graphene such as fluorescence, non-linear optical absorption and surface enhanced Raman scattering (SERS) [3]. Because of the chemically amenable surface and interesting properties, GO has been extensively harnessed as a building block to construct multifunctional nanohybrid structures with functional nanomaterials such as metal and semiconductors [4].

Especially, the hybridization of TiO_2, wide band-gap semiconductor, with GO derivatives has been extensively investigated for its important potential applications such as photocatalysis, photoelectrochemistry, dye-sensitized solar cell, UV protection and self-cleaning coating based on its electron-hole pair separation by UV absorption corresponding to its band gap energy [5–8]. The fabrication of RGO/TiO_2 nanohybrid structures relied on self-assembly, sol-gel processes and photochemical reactions, and the resulting structures have exhibited the significantly enhanced performance for the applications based on the electrical conductivity and electron acceptability of RGO, retarding the electron-hole pair recombination process on TiO_2 [9–12].

The advance in fabrication processes of RGO/TiO_2 nanohybrid structures is of the utmost importance to fully harnessing the unique and excellent properties of RGO and TiO_2 with synergistic effects. The fabrication strategy should be facile, controllable and reproducible for their successful applications. In this regard, the layer-by-layer (LBL) assembly technique is a promising strategy to precisely control the structure of nanohybrid materials by alternative deposition of individual building blocks [13]. This technique has been employed in the in-depth investigation of functional nanohybrid structures for various applications such as drug delivery, transparent electrodes, electrochemical devices, surface-enhanced Raman scattering and laser desorption/ionization mass spectrometry [14–18]. GO derivatives have been also employed for LBL assembly in combination with functional nanomaterials [19–21]. Recently, the fabrication of RGO/TiO_2 nanohybrid thin films was reported by repeated sol-gel reactions of titanium tetrabutoxide inside LBL assembled polydiallyldimethylammonium chloride (PDDA)/RGO

* Corresponding author.
E-mail address: youngkwan@kist.re.kr (Y.-K. Kim).

http://dx.doi.org/10.1016/j.tsf.2017.06.047
0040-6090/

films [22]. Although the nanohybrid films showed interesting multifunctionality including transparency, broadband photoresponse and self-cleaning, this strategy still requires multi-steps of LBL assembly of RGO and poly (diallyldimethylammonium chloride) (PDDA), repeated post-incorporation of TiO_2 precursor, and thermal calcination of the resulting hybrid films which could result in undesired side reactions and structural heterogeneity.

Herein, we demonstrated the simple and controllable fabrication of RGO/TiO_2 nanohybrid films by LBL assembly of polyallylamine-grafted RGO (PAA-RGO) and titanium(IV) bis(ammonium lactato)dihydroxide (TALH) that are precursors for RGO and TiO_2, respectively. Since TALH presented negative charges, it can be directly deposited by LBL process on the charged substrates with positively charged species and converted into TiO_2 by thermal treatment [23]. Therefore, the thickness and surface properties of PAA-RGO and TALH nanohybrid films were precisely controlled within 10 cycles of LBL assembly. The formation process and surface properties of $(PAA\text{-}RGO/TALH)_{1-10}$ nanohybrid films, where the subscript number is the number of LBL assembly cycles, were systematically characterized and the fabricated $(PAA\text{-}RGO/TALH)_{1-10}$ films were thermally treated to convert them into $(RGO/TiO_2)_{1-10}$ films presenting the interesting multifunctional properties such as UV resistance, self-cleaning, controllable electrical conductivity and transparency (Fig. 1). For the best of our knowledge, this is the first example of the direct LBL assembly of functionalized RGO sheets and TiO_2 precursor and thus the RGO/TiO_2 nanohybrid films were straightforwardly fabricated by the subsequent thermal treatment. This simple fabrication process enables to precise manipulation of the structures of resulting RGO/TiO_2 nanohybrid films with controllable and excellent multifunctionality including electrical conductivity, transparency, UV-resistance and self-cleaning.

2. Experimental section

2.1. Materials

Graphite (FP 99.95% pure) was purchased from Graphit Kropfmühl AG (Hauzenberg, Germany). Sodium nitrate, potassium hydroxide and hydrogen peroxide (30% in water) were purchased from Junsei (Japan). 3-glycidylpropyltrimethoxysilane (3-GPTMS), methylene blue (MB), poly(stryrene sulfonate) (PSS), potassium permanganate, anhydrous toluene and PAA (MW 15,000) were purchased from Aldrich Chemical Co. (Milwaukee, WI, USA). Nitric acid and sulfuric acid were purchased from Samchun (Seoul, Korea). Ethanol was purchased from Merck (Darmstadt, Germany). TALH was purchased from Alfa aesar (Ward Hill, MA, USA). Si substrates (500 μm in thickness) and quartz substrates (500 μm in thickness) were purchased from STC (Japan) and i-Nexus (Stamford, USA), respectively. All chemicals were used as received.

2.2. Preparation of GO

3 g of graphite and 1 g of sodium nitrate were added in 46 mL of sulfuric acid and stirred in an ice-bath. Then, 6 g of potassium permanganate was slowly added to the mixture with stirring and the temperature of this reaction mixture was maintained below 20 °C. After finishing the addition, the temperature of the reaction mixture was raised to 35 °C and the mixture was stirred for 1 h. 40 mL of water was then added to the mixture, stirred for 30 min and 100 mL of water was added to the mixture in an ice-bath to prevent rapid boiling. Finally, 6 mL of hydrogen peroxide (30%) was gradually added to the mixture and upon addition, the color of the reaction mixture changed to bright yellow. The mixture was filtered with a filter paper (Number 3, Whatman) and washed with a plenty of water until the filtrate was neutralized. The filtered cake was dried under vacuum for 2 days. The prepared graphite oxide powder was analyzed by FT-IR spectroscopy with a KBr pellet method. The graphene oxide was prepared by sonicating the graphite oxide powder in water (1 mg/mL).

2.3. Synthesis of PAA-RGO sheets

GO was synthesized by Hummers and Offeman's method (for detailed experimental procedure, see supporting information) [24]. The synthesized GO was simultaneously reduced and functionalized with PAA by our previously reported method [25]. In detail, GO (10 mg) was dispersed in 50 mL of water containing 40 mg of PAA, and 50 mg of KOH by sonication for 1 h. The suspension was vigorously stirred at 70 °C for 24 h. After cooling to RT, the PAA-RGO was purified and collected by centrifugation at 8228 rcf for 30 min and re-suspended in water by sonication. The centrifugation and re-suspension processes were repeated three times.

2.4. 3-GPTMS functionalization of a substrate

The quartz and Si substrates were treated in Piranha solution for 10 min at 125 °C, washed with water and ethanol, and dried under a stream of nitrogen. The treated substrates were immersed in a 10 mM anhydrous toluene solution of 3-GPTMS for 30 min, washed with ethanol and water and dried under a stream of nitrogen.

2.5. Fabrication of $(RGO/TiO_2)_n$ films

The 3-GPTMS treated substrates were immersed in PAA-RGO suspension (1 mg/mL) for 30 min, washed with water and ethanol and dried under a stream of nitrogen. The PAA-RGO coated substrates were then immersed in 5% TALH solution for 30 min, washed with water and ethanol and dried under a stream of nitrogen. These processes were repeated up to 10 cycles. The fabricated $(PAA\text{-}RGO/TALH)_n$ thin

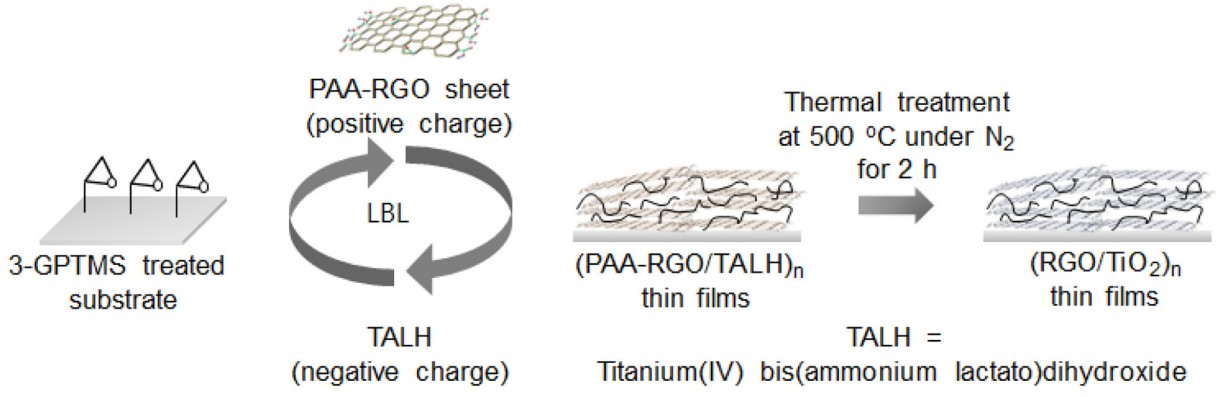

Fig. 1. Fabrication of $(PAA\text{-}RGO/TALH)_n$ thin films by using LBL assembly technique.

films were thermally treated at 500 °C for 2 h under nitrogen atmosphere.

2.6. Fabrication of $(PAA\text{-}RGO/PSS)_n$ films

(PAA-RGO/PSS) thin films were fabricated by LBL assembly of PAA-RGO and PSS. The PAA-RGO coated substrates were immersed in 1 mg/mL PSS solution for 30 min, washed with water and ethanol, and dried under a stream of nitrogen. The $(PAA\text{-}RGO/PSS)_1$ films were immersed in PAA-RGO suspension (1 mg/mL) for 30 min, washed with water and ethanol and dried under a stream of nitrogen. These processes were also repeated up to 10 cycles.

2.7. UV resistant property of $(RGO/TALH)_{10}$ and $(PAA\text{-}RGO/PSS)_{10}$ films

$(PAA\text{-}RGO/TALH)_{10}$ and $(PAA\text{-}RGO/PSS)_{10}$ films were exposed to the UV light (8 W, 254 nm) with 1 cm distance for 5, 10, 20 and 30 min, washed with water and ethanol and dried under a stream of nitrogen.

2.8. Self-cleaning property of $(RGO/TiO_2)_{10}$ films

$(PAA\text{-}RGO/TALH)_{10}$ films were immersed in 1 mM aqueous solution of MB for 12 h, washed with water and ethanol, and dried under a stream of nitrogen. The MB adsorbed $(PAA\text{-}RGO/TALH)_{10}$ films were exposed to UV light (8 W, 254 nm) with 1 cm distance for 5, 10, 20 and 30 min, washed with water and ethanol, and dried under a stream of nitrogen.

2.9. Characterization

The surface morphologies and line profiles were obtained with an XE-100 (Park System, Korea) by using backside gold coated cantilever. The UV–vis spectra were recorded by a UV-2550 (Shimadzu, Japan). Ellipsometric analysis was carried out with a L116S (Gaertner Scientific Corportation, USA). Raman characterization was carried out by LabRAM HR UV/vis/NIR (Horiba Jobin Yvon, France) using an Ar ion CW laser (514.5 nm) as an excitation source focused through a BXFM confocal microscope equipped with an objective lens (50×, numerical aperture = 0.50). The average sheet resistances were obtained by the standard 4 probe method and were measured with a CMT-SR2000 (Changnam Tech, Korea). Zeta potential was measured by zeta sizer Nano ZS90 (Malvern, U.S.A.). Fourier transform infrared (FT-IR) analysis of GO and PAA-RGO was performed with an EQUINOX55 (Bruker, Germany) using the KBr pellet method. Thermogravimetric analysis (TGA) of GO, PAA-RGO and thermally treated PAA-RGO was carried out with TGA S-1000 (SCINCO, Korea).

3. Results and discussion

3.1. Synthesis and characterization of PAA-RGO

GO was synthesized by Hummers' method and characterized by using various spectroscopies including FT-IR, Raman, UV–vis and XPS. FT-IR spectrum of GO showed characteristic peaks from oxygen-containing functional groups such as 1079 cm^{-1} from C—O stretching, 1400 cm^{-1} from O—H deformation, 1627 cm^{-1} from C═C skeletal vibrations of the oxidized graphitic structure, 1716 cm^{-1} from C═O stretching and 3415 cm^{-1} from O—H vibrations (Fig. 2a). The observed peaks from FT-IR spectrum of GO are well matched with our previous report [26]. The Raman spectrum of GO showed typical D- and G-peaks at 1344 and 1608 cm^{-1} corresponding to the A_{1g} mode of sp^3 and the E_{2g} mode of sp^2 carbon domains indicating formation of defects in graphitic structure during the oxidation process [26]. The D- and G-peak intensity ratio (D/G peak) was 0.96 (Fig. 2b) and the Raman analysis results concurred well with the previously reported value of GO [26]. UV–Vis spectrum of GO suspension showed characteristic absorption peak at 231 nm from π-π* transition of aromatic C—C bond (Fig. 2c). The GO was readily dispersed in water by sonication for 1 h and analyzed by atomic force microscopy (AFM). The thickness of GO sheets was 1.05 nm which corresponded to a single layer (Fig. 2d).

For reduction of GO with introducing positive charges, GO was reacted with PAA in the presence of KOH by ring-opening reaction of epoxy functional groups on GO surfaces with amine functional groups of PAA [26]. The reduction and functionalization of GO with PAA were confirmed by FT-IR, Raman and UV–vis spectroscopy. FT-IR spectrum of PAA-RGO showed the drastic structural changes such as weakening of O—H vibration, C—O stretching and disappearing of C═O stretching peaks. Moreover, the aliphatic C—H vibration at 2958 cm^{-1} and CH_3 stretching peaks at 2917 cm^{-1} were enlarged with appearance of C—N stretching at 1257 cm^{-1} and CH_2 bending at 1452 cm^{-1} from covalent bond formation between epoxy groups of GO and primary amine groups of PAA, and long alkyl chain backbone of PAA, respectively

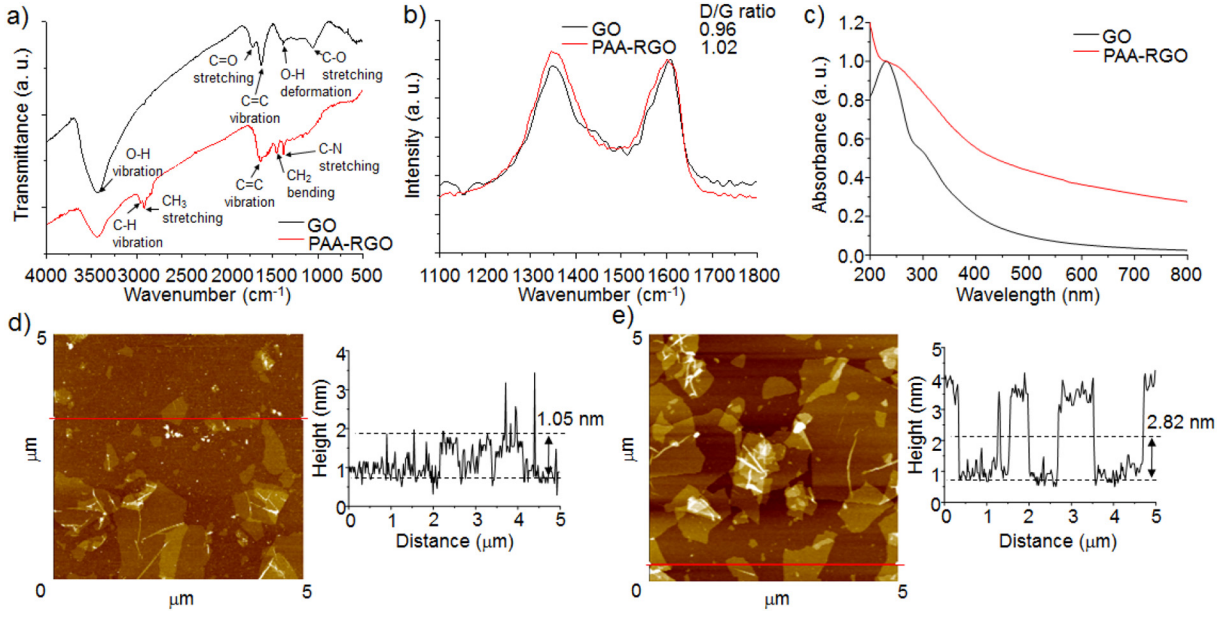

Fig. 2. FT-IR (a), Raman (b) and UV–vis (c) spectra of GO and PAA-RGO. AFM images and line profiles of GO (d) and PAA-RGO (e).

(Fig. 2a). Raman analysis of PAA-RGO also suggested the functionalization based on the increase of D/G peak ratio from 0.96 to 1.02 (Fig. 2b). This degree of increase of D/G peak ratio was also well matched with our previous report [25]. UV–vis spectrum of PAA-RGO exhibited considerably red-shifted π-π* transition peak and increased absorption in visible region compared to GO (Fig. 2c). Those analysis results are well matched with our previous report of PAA-GO synthesis [25]. The thickness of GO sheets also increased from 1.05 to 2.82 nm after PAA induced reduction and functionalization (Fig. 2e).

XPS analysis further confirmed the chemical composition and bonding states between the elements of GO and PAA-RGO. C 1s XPS spectrum of GO presented typical peaks from graphitic carbon, epoxy and hydroxyl, carbonyl and carboxylic groups at 284.5, 286.5, 287.7, and 288.5 eV, respectively (Fig. 3a) [27]. This result supported the successful synthesis of GO composed of abundant epoxy groups that are reactive sites for covalent functionalization of PAA. By contrast, C 1s XPS spectrum of PAA-RGO showed appearance of C—N bond at 285.8 eV with substantially decreasing peak at 286.5 eV from epoxy groups (Fig. 3b). This change clearly indicated that the PAA functionalization of GO proceeded by epoxy-ring opening reaction [28]. N 1s XPS spectrum of PAA-RGO was consisted of pyridinic N, secondary, primary and protonated amines at 398.4, 399.6, 400.5 and 402.1 eV (Fig. 3c) [29,30]. The N 1s XPS spectrum of PAA-RGO clearly revealed the bonding state of N and PAA functionalization of GO mainly occurred by reaction between epoxy groups of GO and primary amine groups of PAA based on the formation of secondary amine bonds on PAA-RGO. Additionally, the C, O and N elemental composition of GO was significantly changed by PAA functionalization from 59.66 to 73.33%, 39.63 to 17.27% and 0.71 to 9.39%, respectively (Fig. 3d). All those characterization results of PAA-RGO clearly confirmed GO was reduced and functionalized by PAA [25–31].

3.2. Fabrication of $(PAA\text{-}RGO/TALH)_n$ films

The synthesized PAA-RGO was readily dispersed in distilled water because of abundant primary amine functional groups on its surface, which present positive charge at neutral pH. It was supported by the positive surface zetapotential of PAA-RGO (46.3 mV) distinct from negative surface zetapotential of GO (−40.7 mV) in phosphate buffered saline (PBS) at pH 7.4. The pH dependent aqueous dispersity of PAA-RGO also supported their positive charges was originated from the primary amine functional groups (Fig. 4) [25,28]. The PAA-RGO sheets were assembled on the surface of 3-glycidoxypropyltrimethoxysilane (3-GPTMS) treated SiO_2/Si substrates by immersing the substrates in PAA-RGO suspension (1 mg/mL) for 30 min. The PAA-RGO coated substrate was subsequently immersed in the 5% TALH solution for 30 min to induce electrostatic adsorption of TALH on the surface immobilized

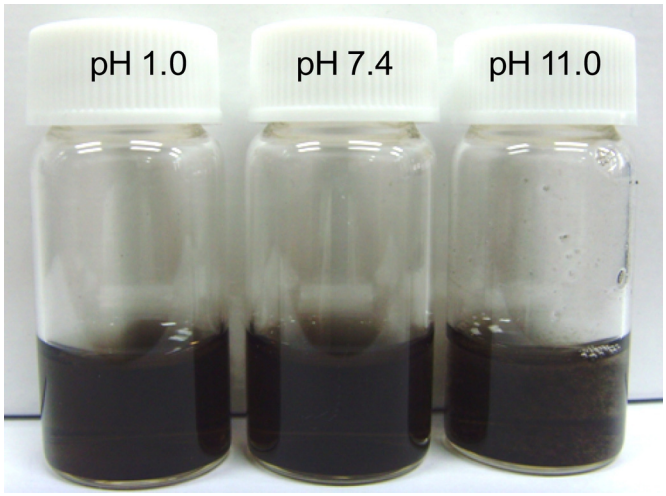

Fig. 4. Photographs of PAA-RGO suspension at different pH value. This result indicated that the PAA-RGO showed the pH-responsive dispersity because the amine groups of PAA-RGO are reversibly protonated and deprotonated according to pH change.

PAA-RGO films. The thickness of PAA-RGO sheets increased from 2.82 to 4.25 nm with TALH adsorption (AFM profile of $(PAA\text{-}RGO/TALH)_1$ film in Fig. 5a). Those results indicate that PAA-RGO sheets and TALH were successfully harnessed as a building block to construct hybrid films by LBL assembly technique.

For the fabrication of PAA-RGO/TALH hybrid films, the 3-GPTMS treated substrates were repeatedly immersed in PAA-RGO aqueous suspension (1 mg/mL) and in 5% TALH aqueous solution up to 10 cycles. The $(PAA\text{-}RGO/TALH)_{1-10}$ films were analyzed by AFM to reveal the changes of surface morphologies and CLA surface roughness with the repeated LBL assembly cycles. The $(PAA\text{-}RGO/TALH)_1$ films showed high surface coverage with TALH adsorbed PAA-RGO sheets and the morphologies were not significantly changed after repeated LBL assembly up to 10 cycles (Fig. 5a). In contrast, the (center line average) CLA surface roughness increased from 2.64 to 14.58 nm with 10 cycles of LBL assembly (Fig. 5b). The growth of $(PAA\text{-}RGO/TALH)_{1-10}$ films was directly monitored by using UV–Vis spectroscopy and ellipsometry. By repeating the LBL assembly cycles of PAA-RGO and TALH on the substrates, the absorbance of $(PAA\text{-}RGO/TALH)_{1-10}$ films gradually increased but the increase was not linear (Fig. 5c). This result concurred with the changes of ellipsometric thickness presenting exponentially increased thickness of $(PAA\text{-}RGO/TALH)_{1-10}$ with LBL assembly cycles. After initial growth of hybrid films with thickness from 4.25 (n = 1) to 9.75 nm (n = 6), the thickness of the hybrid films steeply increased from 21.85 (n = 7) to 42.70 nm (n = 10) (Fig. 5d). This exponential

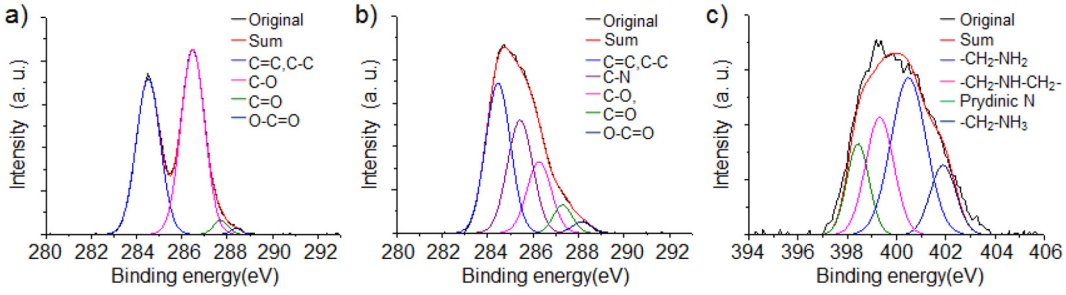

d)

GO			PAA-RGO		
C	O	N	C	O	N
59.66%	39.63%	0.71%	73.33%	17.27%	9.39%

Fig. 3. C 1s XPS spectra of GO (a) and PAA-RGO (b). (c) N 1s XPS spectrum of PAA-RGO and (d) elemental analysis results of GO and PAA-RGO.

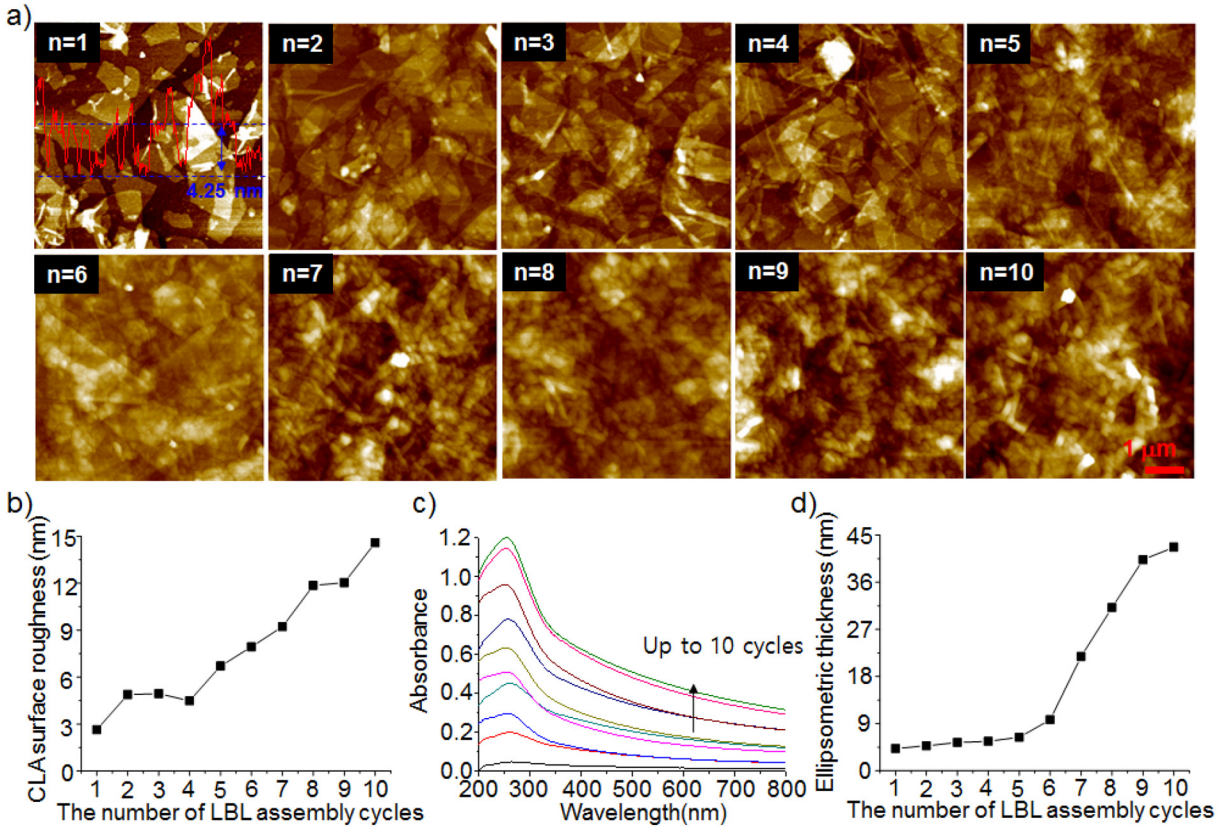

Fig. 5. a) AFM images of $(PAA\text{-}RGO/TALH)_{1-10}$ films with AFM line profile of $(PAA\text{-}RGO/TALH)_1$ film, where the subscript is the number of LBL assembly cycles (1 − 10). b) The UV absorbance changes, c) ellipsometric thickness and d) CLA surface roughness of $(PAA\text{-}RGO/TALH)_{1-10}$ thin films versus the number of LBL assembly cycles.

growth was attributed to the formation of uniform surface charges and linear increase of apparent surface roughness with LBL assembly cycles (Fig. 4a, b) [7,32]. As a result, the growth rate of $(PAA\text{-}RGO/TALH)_n$ films was accelerated after 6 cycles of LBL assembly. Those characterization results indicate that the $(PAA\text{-}RGO/TALH)_n$ films were successfully fabricated with controlled surface properties as a function of the number of LBL assembly cycles.

3.3. Fabrication and characterization of $(RGO/TiO_2)_n$ films

PAA-RGO sheets and TALH in $(PAA\text{-}RGO/TALH)_n$ films were further reduced and hydrolyzed by heating at 500 °C for 2 h under N_2 atmosphere, respectively. Changes in chemical structure of PAA-RGO in the thermal treatment condition were explored by TGA analysis. TGA spectrum of GO showed moderate weight loss of GO around 100 °C and 225 °C was 15.9% and 36.4% from evaporation of adsorbed water and gasification of labile oxygen-containing functional groups on GO. After PAA-functionalization of GO, the weight loss around 100 °C and 225 °C was decreased to 6.7% and 18.0% because of PAA-functionalization induced reduction. Moreover, the additional weight loss (22%) was observed around 450 °C and this point was attributed to thermal degradation of PAA (Fig. 6a). FT-IR spectrum of thermally treated PAA-RGO exhibited the significantly decreased aliphatic C—H stretching peaks and C—N bond stretching peak compared to that of PAA-RGO, which confirmed the most of PAA in the hybrid films was decomposed under our thermal treatment condition (Fig. 6b). This result concurred well with TGA analysis because PAA of PAA-RGO was decomposed at around 450 °C. (Fig. 6a) [23]. The thermally treated $(PAA\text{-}RGO/TALH)_n$ films were called as $(RGO/TiO_2)_n$ films because the PAA was decomposed with conversion of TALH into TiO_2 under this condition. The structural changes of PAA-RGO in $(PAA\text{-}RGO/TALH)_{1-10}$ films by thermal treatment were characterized by using UV–vis and Raman spectroscopies. The UV–vis spectrum of $(PAA\text{-}RGO/TALH)_{10}$ films showed typical absorption peak at 258 nm from π-π* transition of aromatic C—C bonds (Fig. 7a). After

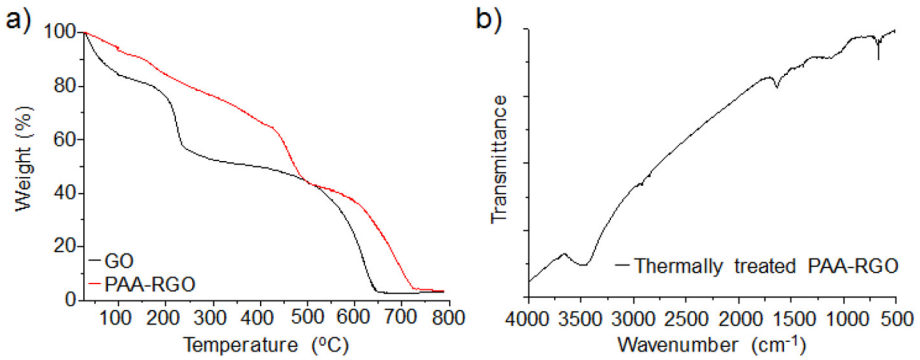

Fig. 6. (a) TGA curves of GO, PAA-GO and thermally treated PAA-GO and (b) FT-IR spectrum of thermally treated PAA-RGO.

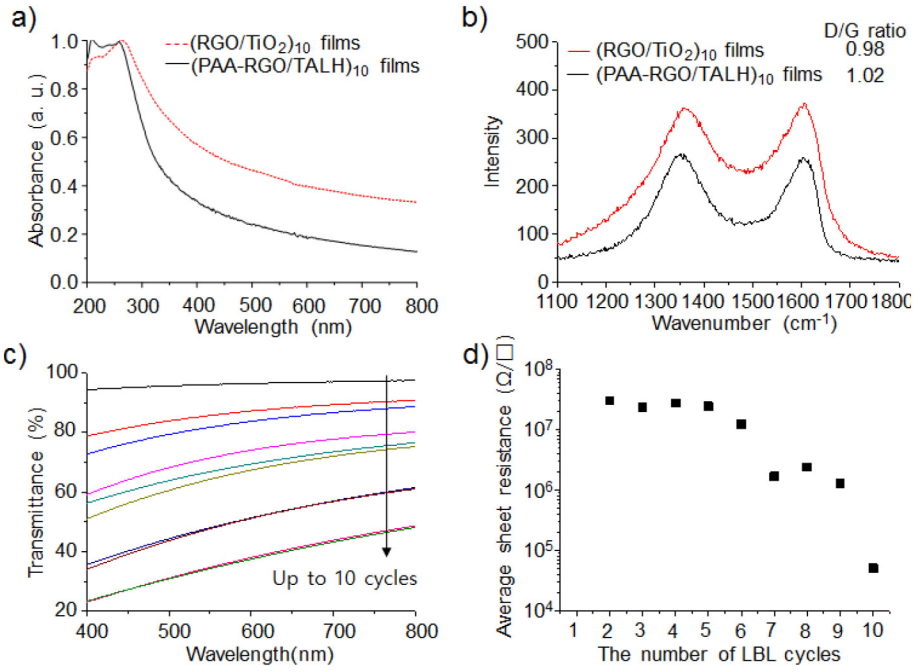

Fig. 7. a) UV–vis and b) Raman spectra of $(PAA\text{-}RGO/TALH)_1$ and $(RGO/TiO_2)_1$. c) Transmittance and d) average sheet resistance of $(RGO/TiO_2)_{1-10}$ thin films as a function of the number LBL assembly cycles.

thermal treatment, the absorption peak of $(RGO/TiO_2)_{10}$ films further red-shifted to 261 nm by heat-induced reduction (Fig. 7a). The Raman spectra of $(PAA\text{-}RGO/TALH)_{10}$ films presented typical D- and G-peaks at 1352 and 1602 cm^{-1} (Fig. 7b) [33]. The relative D/G peak intensity ratio of $(PAA\text{-}RGO/TALH)_{10}$ was 1.04, which is slight higher than that of PAA-RGO, 1.02. This result implied that the defected structures were partially generated in PAA-RGO by the incorporation of TiO_2 precursor during LBL assembly process [12]. After thermal treatment, the D/G peak ratio of $(PAA\text{-}RGO/TALH)_{10}$ films decreased from 1.04 to 0.98 and this change indicated the defected structures of PAA-RGO was restored during thermal treatment (Fig. 7b) [34]. The spectroscopic analysis results suggested that $(PAA\text{-}RGO/TALH)_{10}$ films were successfully converted into $(RGO/TiO_2)_{10}$ films by thermal treatment.

The transparency and electrical conductivity of $(RGO/TiO_2)_{1-10}$ films were then characterized by UV–Vis spectroscopy and standard 4-probe measurement. The transparency of $(RGO/TiO_2)_{1-10}$ films on quartz substrates gradually decreased with repeated LBL assembly cycles from 96.0 to 34.3% at 550 nm (Fig. 7c). The average sheet resistance of $(RGO/TiO_2)_{2-6}$ films on quartz substrates that was obtained from at least five point measurements also gradually decreased from 3.0×10^7 to 1.2×10^7 Ω/sq. After 7 LBL assembly cycles, the average sheet resistance of $(RGO/TiO_2)_{7-10}$ films dramatically decreased from 1.7×10^6 to 5.0×10^4 Ω/sq (Fig. 7d) and this decrease accorded closely with the exponential growth of the $(PAA\text{-}RGO/TALH)_n$ films (Fig. 4). Although the sheet resistance of $(PAA\text{-}RGO/TALH)_{1-10}$ films were over the measurable range because PAA-RGO were separated with the nonconducting PAA and TALH, $(RGO/TiO_2)_{2-10}$ films exhibited the considerable decrease of average sheet resistance by the formation of conductive percolation pathway of RGO sheets by thermal decomposition of PAA and TALH. The average sheet resistance of $(RGO/TiO_2)_{10}$ films was measured as 5.0×10^4 Ω/sq and this value is lower than the reported value of RGO films (1.7×10^5 Ω/sq) prepared by 10 LBL assembly cycles of RGO and PDDA [22]. The relatively low average sheet resistance of $(RGO/TiO_2)_{10}$ films compared to RGO films with intercalated PDDA suggested that the intercalated TiO_2 resulted in lower decrease of conductivity than insulating polymer (PDDA). On the other hand, the average sheet resistance of $(RGO/TiO_2)_{10}$ films was higher than that of RGO films (8.6×10^3 Ω/sq) prepared by 10 LBL assembly cycles of RGO and aminated RGO by ethylenediamine (EDA), which indicated the intercalated TiO_2 lead to higher decrease of conductivity than small organic molecules (EDA) [19]. Based on the comparison, it was confirmed that the prepared $(RGO/TiO_2)_{10}$ films showed comparable electrical conductivity to the literature values of multilayered RGO films prepared by LBL assembly.

3.4. UV resistant property of $(RGO/TiO_2)_{10}$ films

For examination of the origin of UV resistance property, $(PAA\text{-}RGO/PSS)_{10}$ films were prepared by LBL assembly of PAA-RGO and PSS as a control group. Since PSS possesses permanent negative charge, PAA-RGO and PSS were alternately deposited on the substrates by LBL assembly and the successive deposition process was monitored by UV–Vis spectroscopy (Fig. 8). Then, the $(RGO/TiO_2)_{10}$ and $(PAA\text{-}RGO/PSS)_{10}$ films were exposed to UV light (8 W, 254 nm) for 5, 10, 20 and 30 min and analyzed by using UV–Vis spectroscopy to reveal UV induced structural changes. The initial π-π* transition peak of $(RGO/TiO_2)_{10}$ film was observed at 261 nm and this peak was not affected by UV exposure up to 30 min (Fig. 9a). This result implied that the RGO in $(RGO/TALH)_{10}$ films was protected from UV induced oxidation that generally occurs when graphene derivatives were exposed to UV light [35]. The $(PAA\text{-}RGO/PSS)_{10}$ films were exposed to UV light for 5, 10, 20 and 30 min and analyzed. The initial π-π* transition peak was observed at 262 nm and gradually blue-shifted to 257 nm during UV exposure up to 30 min (Fig. 9b). This change implied that the sp^2 carbon domains in $(PAA\text{-}RGO/PSS)_{10}$ film was damaged by UV exposure (Fig. 9c) [36]. This control experiment confirmed that the UV resistant property of $(RGO/TiO_2)_{10}$ film was derived from the incorporated TiO_2.

The average sheet resistance of UV exposed $(RGO/TiO_2)_{10}$ and $(PAA\text{-}RGO/PSS)_{10}$ films was then analyzed to investigate the effect of UV exposure on their electrical conductivity. The initial average sheet resistance of $(RGO/TiO_2)_{10}$ film was around 5.0×10^4 Ω/sq and this value significantly decreased to 2.0×10^4 Ω/sq after UV exposure for 30 min (Fig. 9d). The decrease of average sheet resistance was attributed to the further reduction of RGO induced by photoelectron transfer from TiO_2 [12]. Importantly, $(RGO/TiO_2)_{10}$ films exhibited 2.5 fold decrease of the average sheet resistance after 30 min UV exposure and this

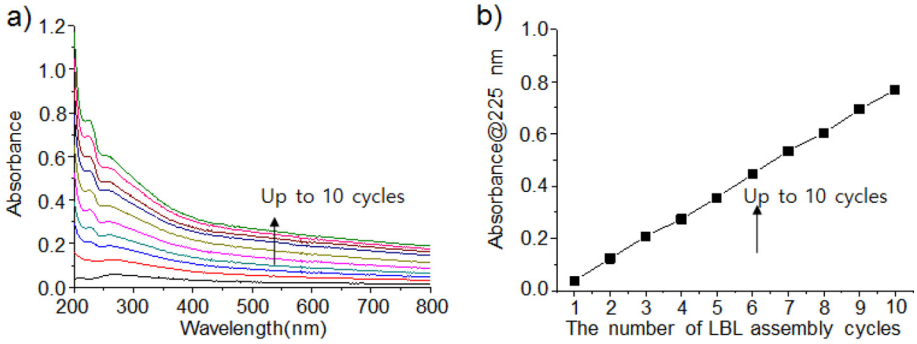

Fig. 8. (a) UV–vis spectra and (b) absorbance at 225 nm of $(PAA\text{-}RGO/PSS)_{1-10}$ films versus the number of LBL assembly cycles. The linear increase of absorbance at 225 nm clearly confirmed the successful fabrication of $(PAA\text{-}RGO/PSS)_{1-10}$ films by LBL assembly cycles.

decrease is considerably higher than our previous report on UV resistant conductive RGO/TiO_2 bi-layered nanohybrid films which showed 1.7 fold decrease of average sheet resistance from 1.0×10^6 to 6.0×10^5 even after 60 min UV exposure [12]. The sharp decrease of average sheet resistance from $(RGO/TiO_2)_{10}$ films can be attributed to the high interfacing area between RGO and TiO_2 based on their alternating structures prepared by LBL assembly. On the other hand, the average sheet resistance of $(PAA\text{-}RGO/PSS)_{10}$ films substantially increased from 5.0×10^4 to 7.5×10^4 Ω/sq after UV exposure for 30 min (Fig. 8d). The increased sheet resistance is in accordance with the typical response of graphene derivatives by UV induced formation of defected structures. Therefore, UV resistant conductive property of $(RGO/TiO_2)_{10}$ film was successfully confirmed with their stable structure and average sheet resistance.

3.5. Self-cleaning property of $(RGO/TiO_2)_{10}$ films

The photocatalytic decomposition of MB on $(RGO/TiO_2)_{10}$ films was examined to demonstrate its self-cleaning property. $(RGO/TiO_2)_{10}$ films were immersed in 1 mM aqueous solution of MB. After incubation, the new absorption bands appeared around 552 nm and 705 nm on $(RGO/TiO_2)_{10}$ films by the adsorption of MB molecules. Then, the $(RGO/TiO_2)_{10}$ films were exposed to UV light (8 W, 254 nm) for 30 min and the absorption of MB completely disappeared with UV exposure time (Fig. 10). This result clearly signified that the $(RGO/TiO_2)_{10}$ films possess the competitive photocatalytic self-cleaning property with the previously reported RGO/TiO_2 hybrid films prepared by spin-coating of RGO and TALH mixture and followed by thermal treatment at 400° [37].

4. Conclusion

We developed an simple, efficient and controllable fabrication strategy of $(RGO/TiO_2)_n$ films by using LBL assembly technique. The thickness and CLA surface roughness of $(PAA\text{-}RGO/TALH)_n$ films were well controlled by simply repeating the LBL assembly cycles of PAA-RGO and TALH. By thermal treatment, the $(PAA\text{-}RGO/TALH)_n$ films were successfully converted into $(RGO/TiO_2)_n$ films with recovery of electrical conductivity. The transparency and average sheet resistance of $(RGO/TiO_2)_n$ films were also dependent on the number of LBL assembly cycles. Importantly, the $(RGO/TiO_2)_{10}$ films presented higher electrical conductivity than LBL assembled films of RGO and cationic polymer, UV resistance than

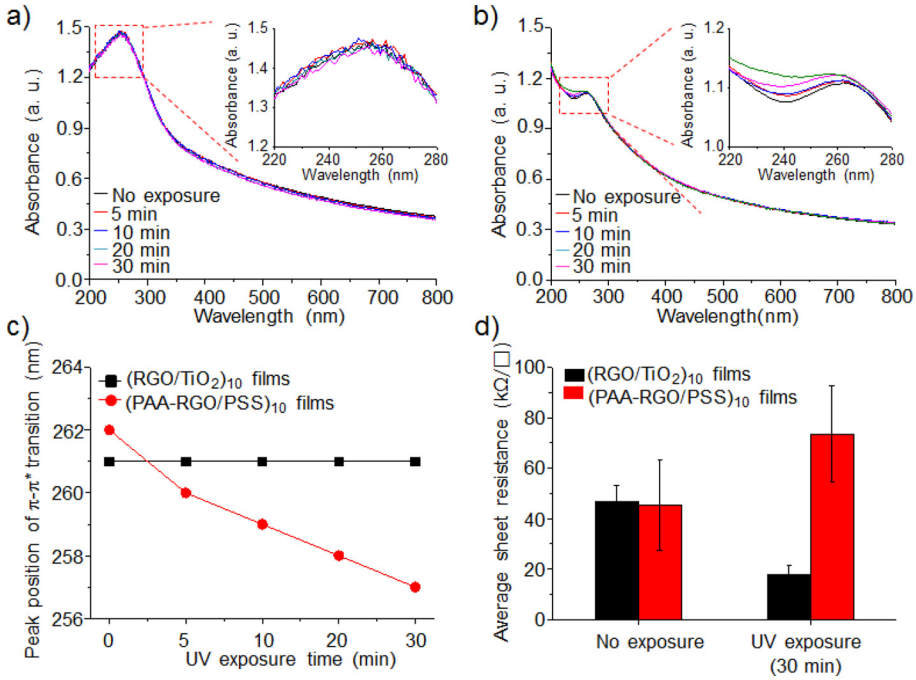

Fig. 9. a) UV–vis spectra of $(RGO/TiO_2)_{10}$ and (PAA-RGO/PSS) b) films with UV exposure time. c) The changes of π-π* transition peak position as a function of UV exposure time. d) The changes of average sheet resistance of $(RGO/TiO_2)_{10}$ and $(PAA\text{-}RGO/PSS)_{10}$ films after 30 min exposure to UV light. The insets of panels a and b clearly showed the changes of π-π* transition peak position of $(RGO/TiO_2)_{10}$ and (PAA-RGO/PSS).

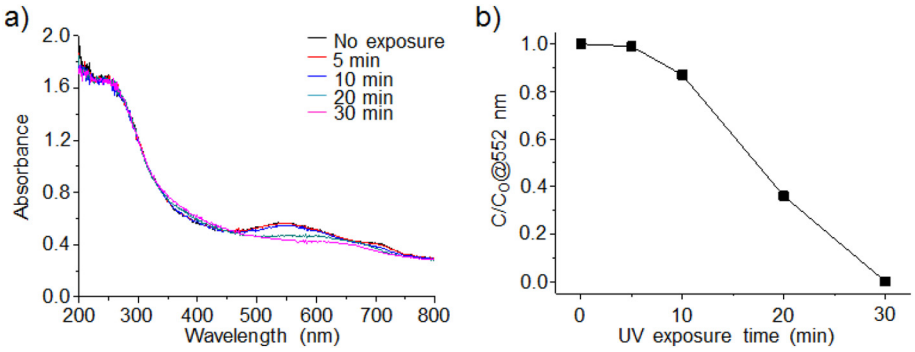

Fig. 10. a) UV–vis spectra of MB adsorbed $(RGO/TiO_2)_{10}$ films with UV exposure time. b) The changes of MB absorbance on $(RGO/TiO_2)_{10}$ films as a function of UV exposure time.

bi-layered RGO/TiO_2 nanohybrid films prepared by incorporation of TiO_2 nanoparticles on RGO films, and competitive self-cleaning property to the randomly hybridized RGO/TiO_2 films prepared by spin-coating and followed by thermal treatment of RGO and TALH. The present fabrication strategy of $(RGO/TALH)_n$ films is simple, cost-effective and reproducible with the controllable multifunctional properties. We believe that the present LBL assembly approach will provide a useful route to fabricate $(RGO/TiO_2)_n$ nanohybrid films on a solid substrate for various applications such as photocatalysis, photoelectrochemistry, DSSC, self-cleaning coating and photochemical synthesis of metal nanostructures.

Notes

The authors declare no competing financial interest.

Acknowledgment

This research was financially supported by grants from the Korea Institute of Science and Technology (KIST) institutional program and Nano·Material Technology Development Program through the National Research Foundation of Korea (NRF) funded by the Ministry of Science, ICT and Future Planning (2016M3A7B4027223) and (2016M3A7B4905609).

References

[1] A.K. Geim, K.S. Novoselov, The rise of graphene, Nat. Mater. 6 (2007) 183–191.
[2] K.P. Loh, Q. Bao, G. Eda, M. Chhowalla, Graphene oxide as a chemically tunable platform for optical applications, Nat. Chem. 2 (2010) 1015–1024.
[3] A. Bagri, C. Mattevi, M. Acik, Y.J. Chabal, M. Chhowalla, V.B. Shenoy, Structural evolution during the reduction of chemically derived graphene oxide, Nat. Chem. 2 (2010) 581–587.
[4] X. Huang, X. Qi, F. Boey, H. Zhang, Graphene-based composites, Chem. Soc. Rev. 41 (2012) 666–686.
[5] Z.Y. Liu, X. Quan, H.B. Fu, X.Y. Li, K. Yang, Effect of embedded-silica on microstructure and photocatalytic activity of titania prepared by ultrasound-assisted hydrolysis, Appl. Catal. B 52 (2004) 33–40.
[6] U. Diebold, The surface science of titanium dioxide, Surf. Sci. Rep. 48 (2003) 53–229.
[7] M. Grätzel, Photoelectrochemical cells, Nature 414 (2001) 338–344.
[8] S.H. Oh, R.R. Finones, C. Daraio, L.H. Chen, S.H. Jin, Growth of nano-scale hydroxyapatite using chemically treated titanium oxide nanotubes, Biomaterials 26 (2005) 4938–4943.
[9] C. Chen, W. Cai, M. Long, B. Zhou, Y. Wu, D. Wu, Y. Feng, Synthesis of visible-light responsive graphene oxide/TiO_2 composites with p/n heterojunction, ACS Nano 4 (2010) 6425–6432.
[10] Y.B. Tang, C.S. Lee, J. Xu, Z.T. Liu, Z.H. Chen, Z. He, Y.L. Cao, G. Yuan, H. Song, L. Chen, L. Luo, H.M. Cheng, W.J. Zhang, I. Bello, S.T. Lee, Incorporation of graphenes in nanostructured TiO_2 films via molecular grafting for dye-sensitized solar cell application, ACS Nano 4 (2010) 3482–3488.
[11] G. Williams, B. Seger, P.V. Kamat, TiO_2-graphene nanocomposites. UV-assisted photocatalytic reduction of graphene oxide, ACS Nano 2 (2008) 1487–1491.
[12] Y.-K. Kim, D.-H. Min, UV protection of reduced graphene oxide films by TiO_2 nanoparticle incorporation, Nanoscale 5 (2013) 3638–3642.
[13] F.X. Xiao, M. Pagliaro, Y.J. Xu, B. Liu, Layer-by-layer assembly of versatile nanoarchitectures with diverse dimensionality: a new perspective for rational construction of multilayer assemblies, Chem. Soc. Rev. 45 (2016) 3088–3121.
[14] S. Correa, E.C. Dreaden, L. Gu, P.T. Hammond, Engineering nanolayered particles for modular drug delivery, J. Control. Release 240 (2016) 364–386.
[15] F.S. Gittleson, D. Hwang, W.H. Ryu, S.M. Hashmi, J. Hwang, T. Goh, A.D. Taylor, Ultrathin nanotube/nanowire electrodes by spin-spray layer-by-layer assembly: a concept for transparent energy storage, ACS Nano 9 (2015) 10005–10017.
[16] Y. Zhang, M.A. Arugula, M. Wales, J. Wild, A.L. Simonian, A novel layer-by-layer assembled multi-enzyme/CNT biosensor for discriminative detection between organophosphorus and non-organophosphrus pesticides, Biosens. Bioelectron. 67 (2015) 287–295.
[17] M. Chen, I.Y. Phang, M.R. Lee, J.K. Yang, X.Y. Ling, Layer-by-layer assembly of Ag nanowires into 3D woodpile-like structures to achieve high density "hot spots" for surface-enhanced Raman scattering, Langmuir 29 (2013) 7061–7069.
[18] Y.-K. Kim, D.-H. Min, Mechanistic study of laser desorption/ionization of small molecules on graphene oxide multilayer films, Langmuir 30 (2014) 12675–12683.
[19] D.W. Lee, T.-K. Hong, D. Kang, J. Lee, M. Heo, J.Y. Kim, B.-S. Kim, H.S. Shin, Highly controllable transparent and conducting thin films using layer-by-layer assembly of oppositely charged reduced graphene oxides, J. Mater. Chem. 21 (2011) 3438–3442.
[20] Y.-K. Kim, D.-H. Min, Fabrication of alternating multilayer films of graphene oxide and carbon nanotube and its application in mechanistic study of laser desorption/ionization of small molecules, ACS Appl. Mater. Interfaces 4 (2012) 2088–2095.
[21] N. Song, D. Jiao, S. Cui, X. Hou, P. Ding, L. Shi, Highly anisotropic thermal conductivity of layer-by-layer assembled nanofibrillated cellulose/graphene nanosheets hybrid films for thermal management, ACS Appl. Mater. Interfaces 9 (2017) 2924–2932.
[22] J. Zhu, Y. Cao, J. He, Facile fabrication of transparent, broadband photoresponse, self-cleaning multifunctional graphene-TiO_2 hybrid films, J. Colloid Interface Sci. 420 (2014) 119–126.
[23] Y.G. Guo, L.J. Wan, C.L. Bai, Gold/titania core/sheath nanowires prepared by layer-by-layer assembly, J. Phys. Chem. B 107 (2003) 5441–5444.
[24] W.S. Hummers, R.E. Offeman, Preparation of graphite oxide, J. Am. Chem. Soc. 80 (1958) 1339.
[25] Y.-K. Kim, D.-H. Min, Simultaneous reduction and functionalization of graphene oxide by polyallylamine for nanocomposite formation, Carbon Lett. 13 (2012) 29–33.
[26] Y.-K. Kim, D.-H. Min, The structural influence of graphene oxide on its fragmentation during laser desorption/ionization mass spectrometry for efficient small-molecule analysis, Chem. Eur. J. 21 (2015) 7217–7223.
[27] X. Fan, W. Peng, Y. Li, X. Li, S. Wang, G. Zhang, F. Zhang, Deoxygenation of exfoliated graphite oxide under alkaline conditions: a green route to graphene preparation, Adv. Mater. 20 (2008) 4490–4493.
[28] S.J. Park, D.A. Dikin, S.T. Nguyen, R.S. Ruoff, Graphene oxide sheets chemically cross-linked by polyallylamine, J. Phys. Chem. C 113 (2009) 15801–15804.
[29] Y. Zhang, C. Chen, G. Wu, N. Guan, L. Li, J. Zhang, One-step hydrothermal amino-grafting of graphene oxide as an efficient solid base catalyst, Chem. Commun. 50 (2014) 4305–4308.
[30] S. Chakraborty, S. Saha, V.R. Dhanak, K. Biswas, M. Barbezat, G.P. Terrasid, A.K. Chakraborty, High yield synthesis of amine functionalized graphene oxide and its surface properties, RSC Adv. 6 (2016) 67916–67924.
[31] M. Herrera-Alonso, A.A. Abdala, M.J. McAllister, I.A. Aksay, R.K. Prud'homme, Intercalation and stitching of graphite oxide with diaminoalkanes, Langmuir 23 (2007) 10644–10649.
[32] T. Serizawa, H. Yamashita, T. Fujiwara, Y. Kimura, M. Akashi, Stepwise assembly of enantiomeric poly(lactide)s on surfaces, Macromolecules 34 (2001) 1996–2001.
[33] Y.-K. Kim, D.-H. Min, Durable large-area thin films of graphene/carbon nanotube double layers as a transparent electrode, Langmuir 25 (2009) 11302–11306.
[34] X. D'ıez-Betriu, S. Alvarez-Garc'ıa, C. Botas, P. Alvarez, J. S'anchez-Marcos, C. Prieto, R. Men'endez, A. de Andr'es, Raman spectroscopy for the study of reduction mechanisms and optimization of conductivity in graphene oxide thin films, J. Mater. Chem. C 1 (2013) 6905–6912.
[35] K.S. Kim, Y. Zhao, H. Jang, S.Y. Lee, J.M. Kim, K.S. Kim, J.H. Ahn, P. Kim, J.Y. Choi, B.H. Hong, Large-scale pattern growth of graphene films for stretchable transparent electrodes, Nature 457 (2009) 706–710.
[36] M.Z. Iqbal, M.W. Iqbal, M.F. Khan, J. Eom, Ultraviolet-light-driven doping modulation in chemical vapor deposition grown graphene, Phys. Chem. Chem. Phys. 17 (2015) 20551–20556.
[37] S. Anandan, T.N. Rao, M. Sathish, D. Rangappa, I. Honma, M. Miyauchi, Superhydrophilic graphene-loaded TiO_2 thin film for self-cleaning applications, ACS Appl. Mater. Interfaces 5 (2013) 207–212.